# UCSF
## UC San Francisco Previously Published Works

**Title**

Combined In Silico and In Vitro Approach Predicts Low Wall Shear Stress Regions in a Hemofilter that Correlate with Thrombus Formation In Vivo

**Permalink**

**Journal**

**ISSN**

**Authors**

Buck, Amanda KW
Groszek, Joseph J
Colvin, Daniel C
et al.

**Publication Date**

**DOI**

Peer reviewed

# Combined *in silico* and *in vitro* approach predicts low WSS regions in a hemofilter that correlate with thrombus formation *in vivo*

**Amanda K. W. Buck**[*,§], **Joseph J. Groszek**[¶], **Daniel C. Colvin**[*], **Sara B. Keller**[†], **Clark Kensinger**[&], **Rachel Forbes**[&], **Seth Karp**[&], **Phillip Williams**[&], **Shuvo Roy**[#], and **William H. Fissell**[¶]

[*]Vanderbilt University Institute of Imaging Science, Department of Radiology and Radiological Sciences, Vanderbilt University Medical Center (VUMC)

[§]Department of Biomedical Engineering, Vanderbilt University

[¶]Nephrology and Hypertension, VUMC

[†]Department of Bioengineering, University of Washington

[&]Department of Surgery, VUMC

[#]Department of Bioengineering & Therapeutic Sciences, University of California San Francisco

## Abstract

A major challenge in developing blood-contacting medical devices is mitigating thrombogenicity of an intravascular device. Thrombi may interfere with device function or embolize from the device to occlude distant vascular beds with catastrophic consequences. Chemical interactions between plasma proteins and bioengineered surface occur at the nanometer scale; however, continuum models of blood predict local shear stresses that lead to platelet activation or aggregation and thrombosis. Here, an iterative approach to blood flow path design incorporating *in silico*, *in vitro*, and *in vivo* experiments predicted the occurrence and location of thrombi in an implantable hemofilter. Low wall shear stress (WSS) regions identified by computational fluid dynamics (CFD) predicted clot formation *in vivo*. Revised designs based on CFD demonstrated superior performance, illustrating the importance of a multi-pronged approach for a successful design process.

## Keywords

hemofilter; hemodynamics; thromobogenicity; bioartificial kidney

Corresponding author: William H. Fissell, M.D., VUMC, 1161 21st Ave South, MCN S-3223, Nashville TN 37232-2372, Phone: 615-322-6976, Fax: 615-343-2605, william.fissell@vanderbilt.edu.

## INTRODUCTION

Chronic kidney failure is associated with significant burden on patient and payor alike. Renal transplant is superior to dialysis with respect to survival, cost, and overall burden of care; however, transplant is severely limited by scarcity of donor organs. Approximately 63% of prevalent patients with end-stage renal disease (ESRD) require hemodialysis as a life-extending therapy,[1] even though transplantation offers a survival advantage over hemodialysis.[2] This persistent unmet need for donor organs has stimulated interest in technology-based approaches for overcoming the scarcity problem in organ transplant.[3–7]

Our team is using a biohybrid approach, combining a high-efficiency, silicon-chip hemofilter as a glomerular analogue and a bioreactor of renal tubule cells to accomplish the metabolic, regulatory, and transport functions of the kidney.[6] This paper describes our approach to an iterative design process that identifies and eliminates potentially thrombogenic flow fields in candidate devices.

First, computational fluid dynamics (CFD) was used to model the flow field through a hemofilter blood path and predict areas of thrombus formation. The CFD results were verified using magnetic resonance imaging (MRI) to measure pulsatile flow through the device *in vitro* to simulate physiologic conditions. After iterative *in silico* and *in vitro* improvements, prototype blood flow paths were machined from polycarbonate. Since the purpose of this study was to minimize flow-induced thrombogenicity, the prototypes were machined to the dimensions of the intact hemofilter but did not contain the silicon nanopore filters. The prototypes were implanted in large animals to test whether locations of *in vivo* thrombus formation agreed with CFD predictions. In this study, we used CFD to model unsteady flow in a blood conduit (Device A), and noticed agreement between regions of low wall shear stress (WSS) and thrombus formation. The shape of the blood conduit was revised to minimize regions of low wall shear stress (Device B) and we observed clot-free flow in 30 day implant studies. To our knowledge, this is the first report of physiologically-relevant blood flow simulations used to minimize thrombogenic potential of a hemofilter design for renal replacement therapy.

## METHODS

### Blood Conduit Design and Manufacturing

Two primary design criteria were defined for the implanted hemofilter device. First, the cross-sectional shape of the blood path needed to transition from the round conduits of vasculature and vascular grafts to the rectangular duct flow of a parallel-plate hemofilter, and back to vasculature. Second, to facilitate surgical anastamosis to artery and vein of similar size, a hilum-like configuration was sought: inflow and outflow conduits antiparallel but within a few centimeters of each other. These conditions are then further constrained by the need to prevent thrombosis and avoid stagnant or recirculating flow. The initial design transformed the flow cross-section between 6 mm diameter pipes and a 7 mm wide rectangular duct in a simple "U" shape (Device A, Figure 1). Wall shear stress is the stress imparted on the conduit wall by the tangentially flowing fluid. Given the relationship between WSS and thrombus formation,[8–11] this parameter is used in design of blood

contacting devices. Consequently, the shape was revised in response to *in silico* and *in vivo* findings to include a helical inlet[12] and a gradual outlet curve (Device B, Figure 1) to reduce the size and duration of low WSS regions. All flow paths were designed in SolidWorks® 2008 x64 Edition (Dassault Systèmes, France), and physical prototypes were milled from biocompatible (ISO10993) LEXAN, Resin HPS6. Pieces were vapor polished and thermally bonded to form the blood flow path (Hayes Manufacturing Services, Sunnyvale, CA).

### Flow Measurement by MR

Device A was imaged using a 63 mm inner diameter quadrature radiofrequency (RF) volume coil inside a Varian 9.4T horizontal bore MRI scanner (Agilent Technologies, Santa Clara, CA). A computer-controlled Masterflex L/S pump driver with dual Easy-Load II pump heads (Cole-Parmer, Vernon Hills, IL) drove pulsatile blood flow through the device, using LabVIEW System Design Software (National Instruments, Austin, TX) to prescribe cyclic flow parameters over a period of 560 ms (Figure 2). A pneumatic pillow was used to trigger MR image acquisition. To reduce the longitudinal magnetization relaxation time, a 2 mL dose of gadopentetate dimeglumine (Magnevist, Bayer HealthCare Pharmaceuticals, Inc., Wayne, NJ) was added to the approximately 500 mL of citrated bovine blood (Lampire Biological Laboratories, Pipersville, PA) pumped through the device, improving the signal to noise ratio of the images.

Phase contrast MR (PC-MR) data were acquired in the through-plane direction using a velocity-encoded spoiled gradient echo sequence for "axial" slices (i.e. bulk flow direction at the inlet and outlet was normal to the slice). Imaging parameters included: repetition time=700 ms; field of view = 38.4 mm×9.6 mm; slice thickness = 1mm; voxel size = $0.15 \times 0.15 \times 1$ mm$^3$. The velocity encoding (VENC) parameter was 150 cm/s. To correct for background phase effects due to field inhomogeneity, two sets of images were collected for each velocity-encoding direction, with the polarity of the bipolar velocity-encoding gradients reversed between acquisitions. Following the trigger signal, a series of images collected for 16 cine time points described the pulsatile flow at a temporal resolution of 35 ms.

Following data acquisition, images and two-dimensional phase maps were reconstructed using MATLAB (The Mathworks) and ITK-SNAP,[13] and velocity maps were calculated following phase subtraction of the two acquisitions. Velocity encoding aliasing was addressed using a phase unwrapping algorithm.[14] Through-plane MR velocity data were imported into tec360 (Tecplot, Inc.) for comparison with simulation data.

### *In Vivo* Experiments

All animal experiments were approved by Vanderbilt University's Institutional Animal Care and Use Committee. Devices were implanted in 12 25–30 kg, mixed breed, female Class A dogs: five Device A, and seven Device B (multiple channel heights; Table 1). The 2–3 cm long externally supported polytetrafluoroethylene (PTFE) grafts were attached by end-to-side anastomoses from aorta to device inlet and from inferior vena cava to device outlet. After blood flow was established, the device was secured to the psoas muscle adjacent to the inferior pole of the left kidney. Intravenous heparin (100 units/kg) was administered during

the operation, with an additional 1000 units administered when creating the arterial anastomosis. Post-operatively, the dogs received either Lovenox (0.5mg/kg) once each day or antiplatelet therapy with 1.5 mg/kg acetylsalicylic acid (ASA) per day (Table 1). Blood flow through the grafts was assessed weekly by Doppler ultrasound. Devices were explanted if flow was not detected, or at the end of planned experiment (24–31 days; Table 1).

## Computational Fluid Dynamics Simulations

**Model Construction—**The computational geometry and grid were constructed using ICEM-CFD (ANSYS, Inc.), and laminar simulations were conducted in Fluent v. 15 (ANSYS, Inc.). Entrance and exit lengths were appended to the device geometry to ensure fully developed flow. The computational volume was discretized using tetrahedral elements and three layers of thin, rectangular prism elements at the near wall region to improve boundary layer and WSS estimations.

Grid independence was confirmed when an approximately 50% increase in element number between grids produced a relative error of maximum WSS less than 5% and a maximum velocity relative error at the outlet less than 3%. For all simulations, blood was considered a Newtonian fluid, which is reasonable for the scale of these devices,[15,16] with a density of 1053 kg/m$^3$ and an absolute viscosity of 0.00368 kg/m-s.

**Simulation of *In Vitro* Experiment—**For simulation of the *in vitro* experiment, inlet boundary conditions were based on MR-measured velocities obtained near the inlet of the device. Cine velocimetry measurements were interpolated in MATLAB to produce a volumetric waveform describing blood flow (Figure 2). The median Reynolds number was 260, and the Womersley number was 3.1. Three cycles were concatenated, allowing investigation of temporal convergence. The volumetric flow rate was imposed as the inlet boundary condition of the simulation; the outlet was prescribed as having zero diffusion flux; and the geometry was considered a rigid boundary. Visualization of results was performed using Fluent and Tec360 (Tecplot, Inc.).

Comparisons were made between CFD-calculated, through-plane velocity maps and MR-measured velocity data. The CFD data were extracted from the inlet and outlet faces of the computational geometry. The MR data were acquired from the slice closest to the inlet/outlet of the device and positioned inside the device. Comparisons were made at five time points in the cycle at which the MR and exported CFD data aligned temporally; these included data at the initial time point and peak flow through the device.

**Simulation of *In Vivo* Experiment—**For Device A, representative, ultrasound-measured centerline velocity data were obtained in a graft immediately proximal to an implanted device. Discrete points from the measured velocity waveform were interpolated in MATLAB. The median Reynolds number was 600, and the Womersley number was 3.1. This waveform was used to approximate the flow rate[17] and was imposed as the transient inlet boundary condition. The outlet was prescribed as having zero diffusion flux, and the geometry was considered a rigid boundary. Since resistance of the device is expected to change with geometry revisions, for Device B, an inlet pressure waveform measured in dogs[18] defined the inlet boundary condition; the outlet pressure was defined as 5 mmHg, and

rigid boundaries were assumed. The median Reynolds number/Womersley number pairs were 770/0.8, 1330/1.2, 1680/1.6, and 1870/2.6 for the 500, 750, 1000, and 2000 μm channel-width devices, respectively. The pulsatile simulation was performed over three cardiac cycles to verify temporal convergence.

## RESULTS

### Simulated and Measured Flows *In Vitro*

We compared velocity maps to test agreement between simulations and experiment. Figures 3 and 4 show inlet and outlet velocity contours at approximately the same locations for the *in vitro* and *in silico* models. Both CFD and MR results indicate a parabolic inflow velocity profile over time and a skewed outlet velocity profile. The mean maximum axial velocity errors were 8.9% and 10.4% at the inlet and outlet planes, respectively. The velocity maps demonstrate qualitative agreement between CFD simulations and *in vitro* measurements.

### Simulated Flows and Thrombus Formation *In Vivo*

Given the relationship between shear and thrombogenicity, simulated time-averaged wall shear stress (TAWSS) maps were constructed. The CFD-simulated TAWSS demonstrates locally low WSS regions at the outer wall of the proximal curve and at the inner wall of the distal curve (Figure 5). Due to high WSS values during systolic acceleration, the TAWSS maps obscure regions of persistently low WSS. Mean WSS patterns averaged over the cardiac cycle excluding systolic acceleration demonstrate larger zones of low WSS (Figure 6). In Device B, the zones of low TAWSS are smaller than those seen in Device A, and the location of low TAWSS *foci* varies with channel height (Figure 7).

In Device A, clots developed in three of five implants; however, in Device B, no clots were revealed upon explant (Table 1). Clots in two of the Device A prototypes were identified as residing and/or originating at sites corresponding to regions of low TAWSS and low mean WSS (Figures 5 and 6) identified in the CFD simulations. Figure 8 shows an extracted clot with a platelet-dominated portion formed in the inner wall region of the distal curve. The location corresponds to CFD-simulated regions of low WSS, particularly over the non-systolic acceleration portions of the cycle (Figure 6). This platelet-dominated, pale region likely marks the region of thrombus initiation.

In Device B no thrombi were observed in the experiments. (Figure 7). Notably, although the simulated low TAWSS loci changed with channel height in Device B, no clots developed *in vivo*, indicating the revised design performs well for the range of channel heights.

## DISCUSSION

Device hemodynamics influence coagulation, platelet activation, and eventual thrombosis (e.g.[8–11,19,20]). The accurate prediction of flow fields is an essential step in design of blood-contacting devices.[8–11,21–28] Zones of low WSS can accompany recirculation areas or separation regions, beyond which flow reattachment convects platelets toward the surface.[11] The combination of slow flow and physical forcing of platelet-surface interaction is a powerful stimulus for clot formation.

Distributions of WSS are a function of geometry, blood flow rate and pulsatility. Early investigations demonstrated the importance of studying hemodynamics in the context of physiological conditions[29]. Our implantable bioartificial kidney relies on cardiac perfusion for blood circulation. We hypothesized that simulating *in vivo* conditions when integrating CFD in the device design cycle would reduce thrombosis. The simulations based on physiologic flows agreed with *in vivo* observed thrombus location. Design modifications eliminating areas of low WSS also eliminated device thrombosis over a 30-day implant period. To our knowledge, this is the first investigation of hemodynamics in a cardiac pressure-driven hemofilter using physiologic flow conditions.

Shear loading experienced by platelets traversing intravascular devices causes long-term platelet activation.[30] While the fluid shear stresses in our device are below hemolysis thresholds,[6] subhemolytic levels of shear may prime platelets for local or distant thrombosis. Lagrangian and Eulerian approaches for calculating platelet damage [28,31,32] and platelet residence time calculations may improve future thrombogenicity assessments[33].

Our study is limited by the techniques used. Due to constraints of MR measurement and registration with CFD-calculated values, the locations of the inlet and outlet comparison planes were not identical in the measured and simulated data sets. Additionally, use of human viscosity values to simulate flow of citrated bovine blood may have resulted in velocity estimation errors. In the absence of *in vivo* pressure data, use of the diffusion flux boundary condition also may have contributed to discrepancies between measured and simulated velocity fields. A laminar model was used for these simulations. The vast majority of physiological flows are laminar, but notable exceptions include arteriovenous grafts[34], severe stenosis[35], valve disease[36], and mechanical heart valves[37]. Although instantaneous peak flows may reach Reynolds numbers associated with transitional flow under steady state conditions, they do not necessarily produce instabilities in pulsatile flow. Trip *et al.* (2012)[38] demonstrated that for oscillating flow in a pipe, laminar flow persisted at mean Reynolds numbers higher than those investigated in this study. Further, they found that in the transition region, transitional flow was independent of Womersley number, contrary to previous works (e.g. [39,40]). It should be noted, that the Trip *et al.* study examined pipe flow. While the geometries we considered are more complicated than pipe flow, our devices do not have sudden expansions.

The simulations presented here estimate hemodynamic parameters at high spatiotemporal resolution. Inclusion of *in vivo* and *in vitro* experiments allow demonstration of phenomena that models cannot predict, such as the accumulation of blood components on membranes and how this may induce a sieving effect or formation of clotting precursors. This underscores the utility of a combined *in silico* and *in vivo/in vitro* experimental approach when designing intravascular devices.

## CONCLUSION

This study employed a combination of *in vivo*, *in vitro*, and *in silico* approaches to identify potential fluid dynamics contributors to thrombogenicity in an implantable hemofilter design under realistic operating conditions and to guide future device iterations. The results

demonstrate both the feasibility and the utility of such a combined approach in developing intra-vascular, bioartificial, organ-replacement devices.

## Acknowledgments

## References

1. U.S. Renal Data System. USRDS 2016 Annual Data Report: Epidemiology of Kidney Disease in the United States. Bethesda, MD: 2016.

2. Wolfe RA, Ashby VB, Milford EL, et al. Comparison of Mortality in All Patients on Dialysis, Patients on Dialysis Awaiting Transplantation, and Recipients of a First Cadaveric Transplant. N Engl J Med. 1999; 341:1725–1730. [PubMed: 10580071]

3. Song JJ, Guyette JP, Gilpin SE, Gonzalez G, Vacanti JP, Ott HC. Regeneration and experimental orthotopic transplantation of a bioengineered kidney. Nat Med. 2013; 19:646–51. [PubMed: 23584091]

4. Abolbashari M, Agcaoili SM, Lee M-K, et al. Repopulation of porcine kidney scaffold using porcine primary renal cells. Acta Biomater. 2016; 29:52–61. [PubMed: 26596567]

5. Lanza RP, Chung HY, Yoo JJ, et al. Generation of histocompatible tissues using nuclear transplantation. Nat Biotechnol. 2002; 20:689–696. [PubMed: 12089553]

6. Kensinger C, Karp S, Kant R, et al. First Implantation of Silicon Nanopore Membrane Hemofilters. ASAIO J. 2016; 62:491–495. [PubMed: 26978710]

7. Fissell WH, Manley S, Westover A, Humes HD, Fleischman AJ, Roy S. Differentiated Growth of Human Renal Tubule Cells on Thin-Film and Nanostructured Materials. ASAIO J. 2006; 52:221–227. [PubMed: 16760708]

8. Hochareon P, Manning KB, Fontaine AA, Tarbell JM, Deutsch S. Correlation of in vivo clot deposition with the flow characteristics in the 50 cc penn state artificial heart: a preliminary study. ASAIO J. 50:537–42. [PubMed: 15672785]

9. Topper SR, Navitsky MA, Medvitz RB, et al. The Use of Fluid Mechanics to Predict Regions of Microscopic Thrombus Formation in Pulsatile VADs. Cardiovasc Eng Technol. 2014; 5:54–69. [PubMed: 24634700]

10. Yin W, Alemu Y, Affeld K, Jesty J, Bluestein D. Flow-induced platelet activation in bileaflet and monoleaflet mechanical heart valves. Ann Biomed Eng. 2004; 32:1058–66. [PubMed: 15446502]

11. Duraiswamy N, Cesar JM, Schoephoerster RT, Moore JE. Effects of stent geometry on local flow dynamics and resulting platelet deposition in an in vitro model. Biorheology. 2008; 45:547–61. [PubMed: 19065004]

12. Caro CG, Seneviratne A, Heraty KB, et al. Intimal hyperplasia following implantation of helical-centreline and straight-centreline stents in common carotid arteries in healthy pigs: influence of intraluminal flow†. J R Soc Interface. 2013; 10

13. Yushkevich PA, Piven J, Hazlett HC, et al. User-guided 3D active contour segmentation of anatomical structures: Significantly improved efficiency and reliability. Neuroimage. 2006; 31:1116–1128. [PubMed: 16545965]

14. Ghiglia, DC., Pritt, MD. Two-dimensional phase unwrapping: theory, algorithms, and software. Wiley; 1998.

15. Pries AR, Neuhaus D, Gaehtgens P. Blood viscosity in tube flow: dependence on diameter and hematocrit. Am J Physiol. 1992; 263:H1770–8. [PubMed: 1481902]

16. Lee S-W, Steinman DA. On the Relative Importance of Rheology for Image-Based CFD Models of the Carotid Bifurcation. J Biomech Eng. 2007; 129:273. [PubMed: 17408332]

17. Womersley JR. Method for the calculation of velocity, rate of flow and viscous drag in arteries when the pressure gradient is known. J Physiol. 1955; 127:553–63. [PubMed: 14368548]

18. Olson RM. Aortic blood pressure and velocity as a function of time and position. J Appl Physiol. 1968; 24

19. Moake JL, Rudy CK, Troll JH, et al. von Willebrand factor abnormalities and endothelial cell perturbation in a patient with acute thrombotic thrombocytopenic purpura. Am J Med Sci. 1986; 291:47–50. [PubMed: 3079954]

20. Sakariassen KS, Joss R, Muggli R, et al. Collagen type III induced ex vivo thrombogenesis in humans. Role of platelets and leukocytes in deposition of fibrin. Arteriosclerosis. 10:276–84.

21. Lee JC, Lee K, Kim HC. Mathematical analysis for internal filtration of convection-enhanced high-flux hemodialyzer. Comput Methods Programs Biomed. 2012; 108:68–79. [PubMed: 22325241]

22. Pelosi A, Sheriff J, Stevanella M, Fiore GB, Bluestein D, Redaelli A. Computational evaluation of the thrombogenic potential of a hollow-fiber oxygenator with integrated heat exchanger during extracorporeal circulation. Biomech Model Mechanobiol. 2014; 13:349–361. [PubMed: 23053595]

23. Rambod E, Beizai M, Rosenfeld M. An experimental and numerical study of the flow and mass transfer in a model of the wearable artificial kidney dialyzer. Biomed Eng Online. 2010; 9:21. [PubMed: 20497572]

24. Ge L, Leo H-L, Sotiropoulos F, Yoganathan AP. Flow in a mechanical bileaflet heart valve at laminar and near-peak systole flow rates: CFD simulations and experiments. J Biomech Eng. 2005; 127:782–97. [PubMed: 16248308]

25. Chiu W-C, Slepian MJ, Bluestein D. Thrombus Formation Patterns in the HeartMate II Ventricular Assist Device. ASAIO J. 2014; 60:237–240. [PubMed: 24399065]

26. Li Z, Kleinstreuer C. Analysis of biomechanical factors affecting stent-graft migration in an abdominal aortic aneurysm model. J Biomech. 2006; 39:2264–2273. [PubMed: 16153654]

27. Loth F, Jones SA, Giddens DP, Bassiouny HS, Glagov S, Zarins CK. Measurements of velocity and wall shear stress inside a PTFE vascular graft model under steady flow conditions. J Biomech Eng. 1997; 119:187–94. [PubMed: 9168395]

28. Morbiducci U, Ponzini R, Nobili M, et al. Blood damage safety of prosthetic heart valves. Shear-induced platelet activation and local flow dynamics: A fluid–structure interaction approach. J Biomech. 2009; 42:1952–1960. [PubMed: 19524927]

29. Ku DN, Giddens DP. Pulsatile flow in a model carotid bifurcation. Arteriosclerosis. 3:31–9. [PubMed: 6824494]

30. Bluestein D, Niu L, Schoephoerster RT, Dewanjee MK. Fluid mechanics of arterial stenosis: Relationship to the development of mural thrombus. Ann Biomed Eng. 1997; 25:344–356. [PubMed: 9084839]

31. Marom G, Bluestein D. Lagrangian methods for blood damage estimation in cardiovascular devices - How numerical implementation affects the results. Expert Rev Med Devices. 2016; 13:113–122. [PubMed: 26679833]

32. Hansen KB, Arzani A, Shadden SC. Mechanical Platelet Activation Potential in Abdominal Aortic Aneurysms. J Biomech Eng. 2015; 137:41005.

33. Esmaily-Moghadam M, Hsia T-Y, Marsden AL. A non-discrete method for computation of residence time in fluid mechanics simulations. Phys Fluids. 2013; 25:110802.

34. Loth F, Fischer PF, Bassiouny HS. Blood Flow in End-to-Side Anastomoses *. Annu Rev Fluid Mech. 2008; 40:367–93.

35. Lee SE, Lee S-W, Fischer PF, Bassiouny HS, Loth F. Direct numerical simulation of transitional flow in a stenosed carotid bifurcation. J Biomech. 2008; 41:2551–61. [PubMed: 18656199]

36. Stein PD, Sabbah HN. Turbulent blood flow in the ascending aorta of humans with normal and diseased aortic valves. Circ Res. 1976; 39:58–65. [PubMed: 776437]

37. Yoganathan AP, Chandran KB, Sotiropoulos F. Flow in Prosthetic Heart Valves: State-of-the-Art and Future Directions. Ann Biomed Eng. 2005; 33:1689–1694. [PubMed: 16389514]

38. Trip R, Kuik DJ, Westerweel J, Poelma C. An experimental study of transitional pulsatile pipe flow. Phys Fluids. 2012; 24:14103.

39. Nerem RM, Seed WA. An in vivo study of aortic flow disturbances. Cardiovasc Res. 1972; 6:1–14. [PubMed: 5014275]

40. Falsetti HL, Carroll RJ, Swope RD, Chen CJ. Turbulent blood flow in the ascending aorta of dogs. Cardiovasc Res. 1983; 17:427–36. [PubMed: 6883418]
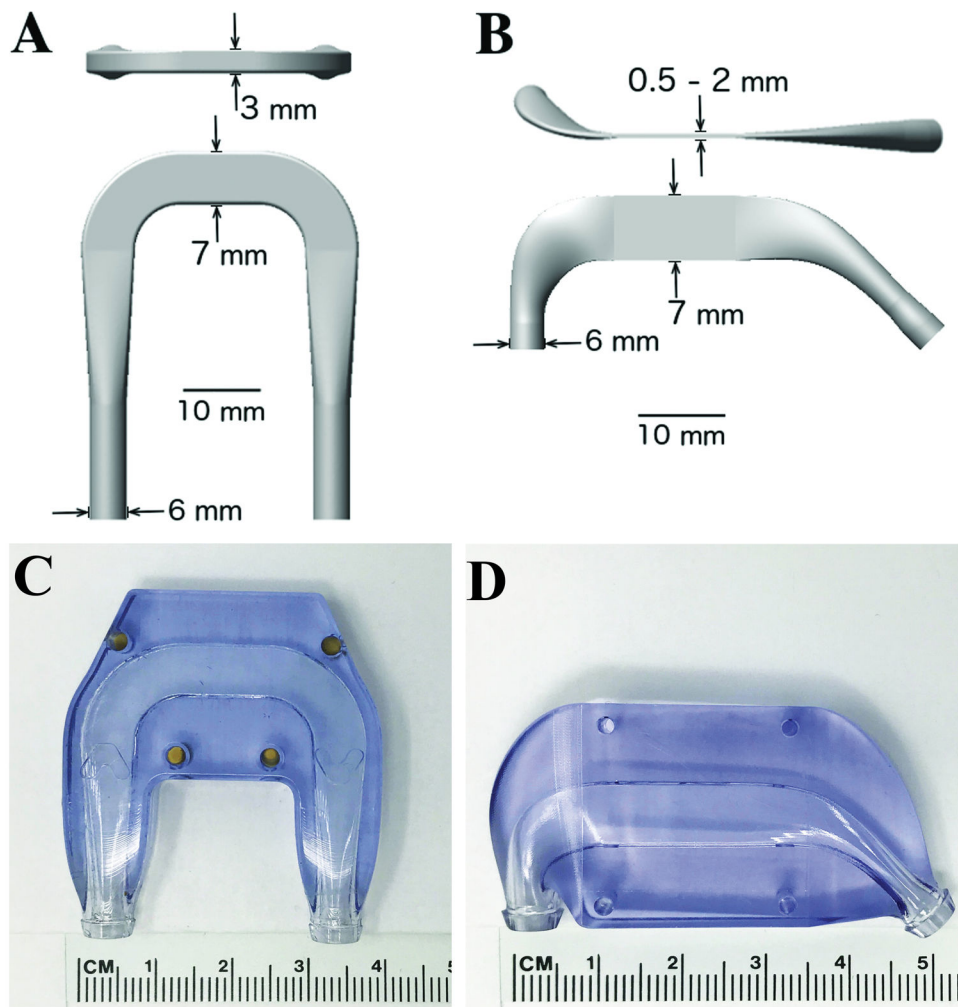
**Figure 1.**
Orthogonal views of the computational geometry used in simulations for Device A (Panel A) and Device B with 500 μm channel (Panel B) are shown. Manufactured flow paths are shown in Panels C and D.
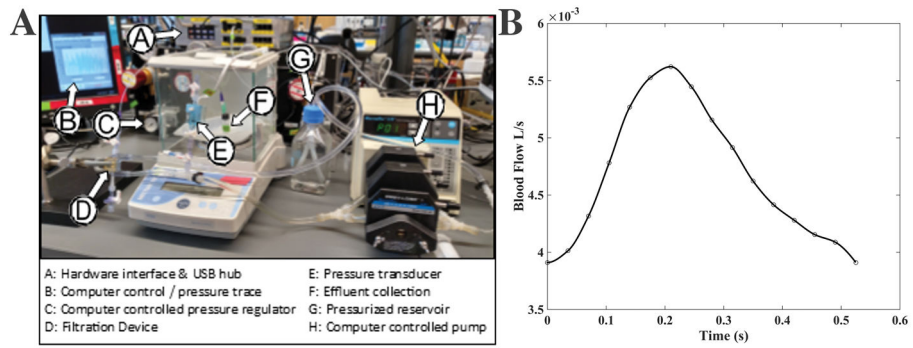
**Figure 2.**
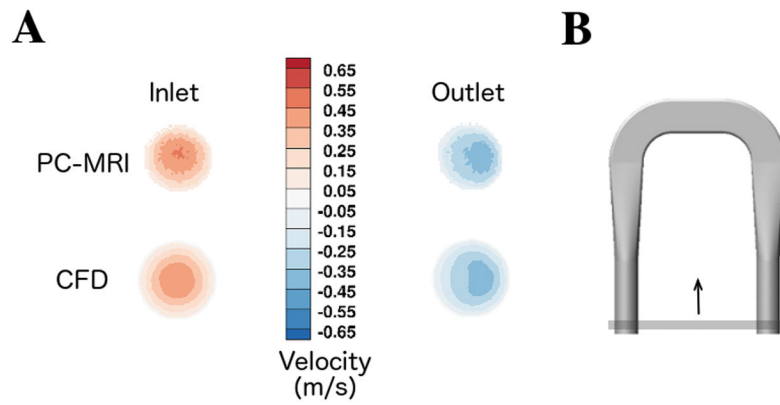A) *In vitro* flow loop. B) Pump mass flow rate measured via PC-MR velocimetry (triangles) and interpolated (line).

**Figure 3.**
A) Through-plane velocity (m/s) comparison for PC-MRI measurements *in vitro* and CFD simulations at the flow rate at the beginning of the cycle. Contours at the inlet and outlet are presented, and positive/negative velocity values demonstrate relative direction of flow. B) Schematic showing approximate MR acquisition plane and orientation.
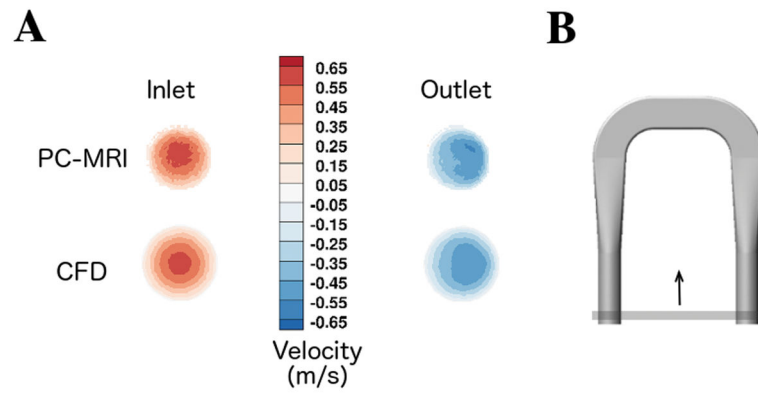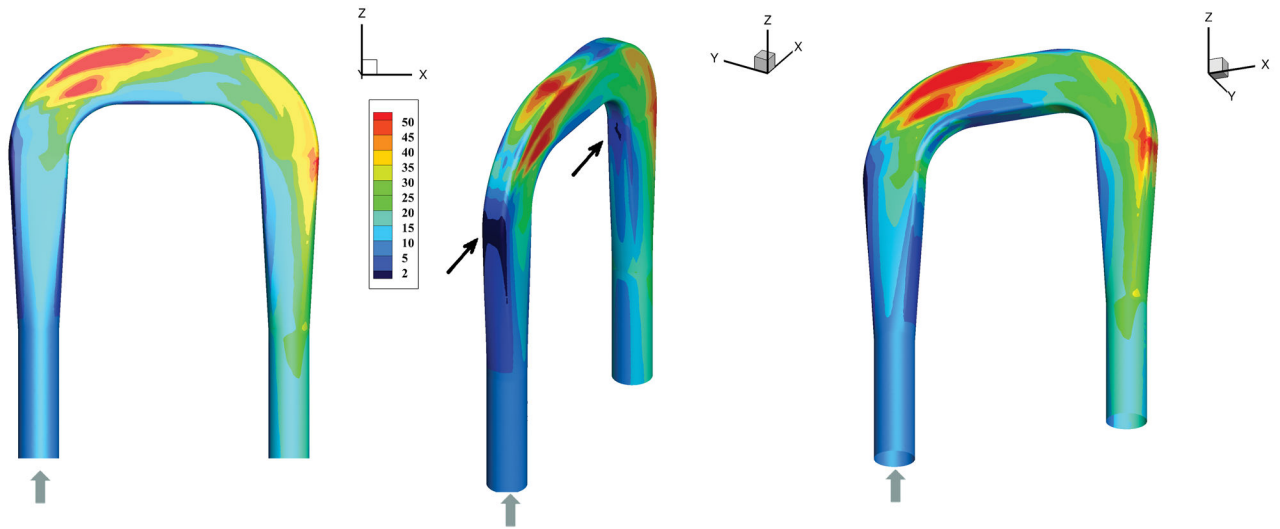
**Figure 4.**
A) Through-plane velocity (m/s) comparison for PC-MRI measurements *in vitro* and CFD simulations at the peak flow rate. Contours at the inlet and outlet are presented, and positive/negative velocity values demonstrate relative direction of flow. B) Schematic showing approximate MR acquisition plane and orientation.

**Figure 5.**
For the simulation of *in vivo* conditions for Device A, three views are shown of the time averaged wall shear stress (TAWSS) map (Pa) from CFD simulations. Grey arrows indicate inflow region of the device, and black arrows indicate regions of locally low TAWSS.
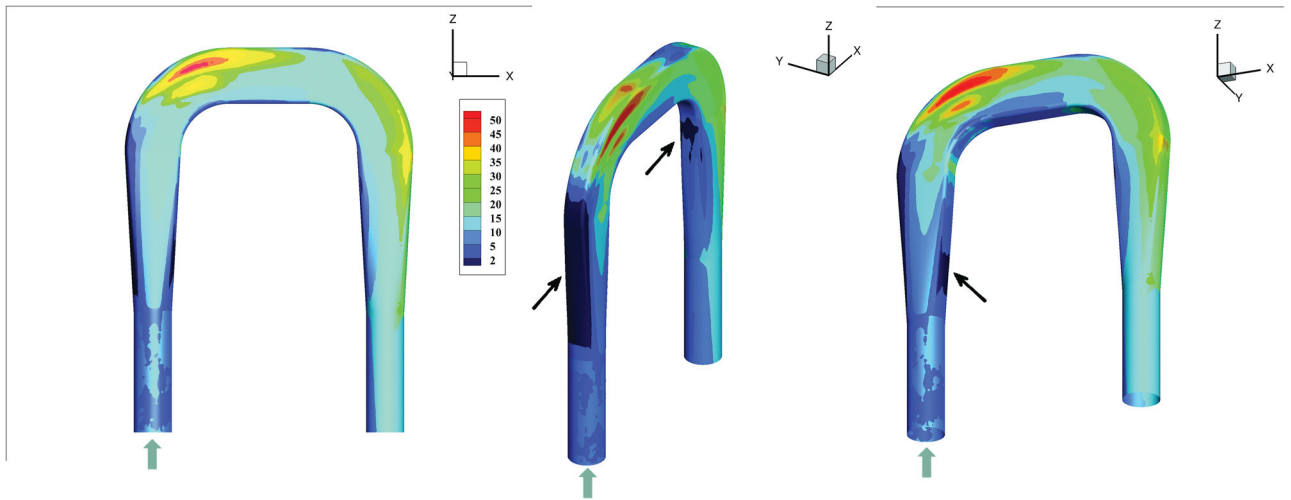
**Figure 6.**
For the simulation of *in vivo* conditions for Device A, three views are shown of the mean wall shear stress (WSS; in Pa) calculated for the portion of the cardiac cycle excluding systolic acceleration. Grey arrows indicate inflow region of the device, and black arrows indicate regions of locally low WSS.
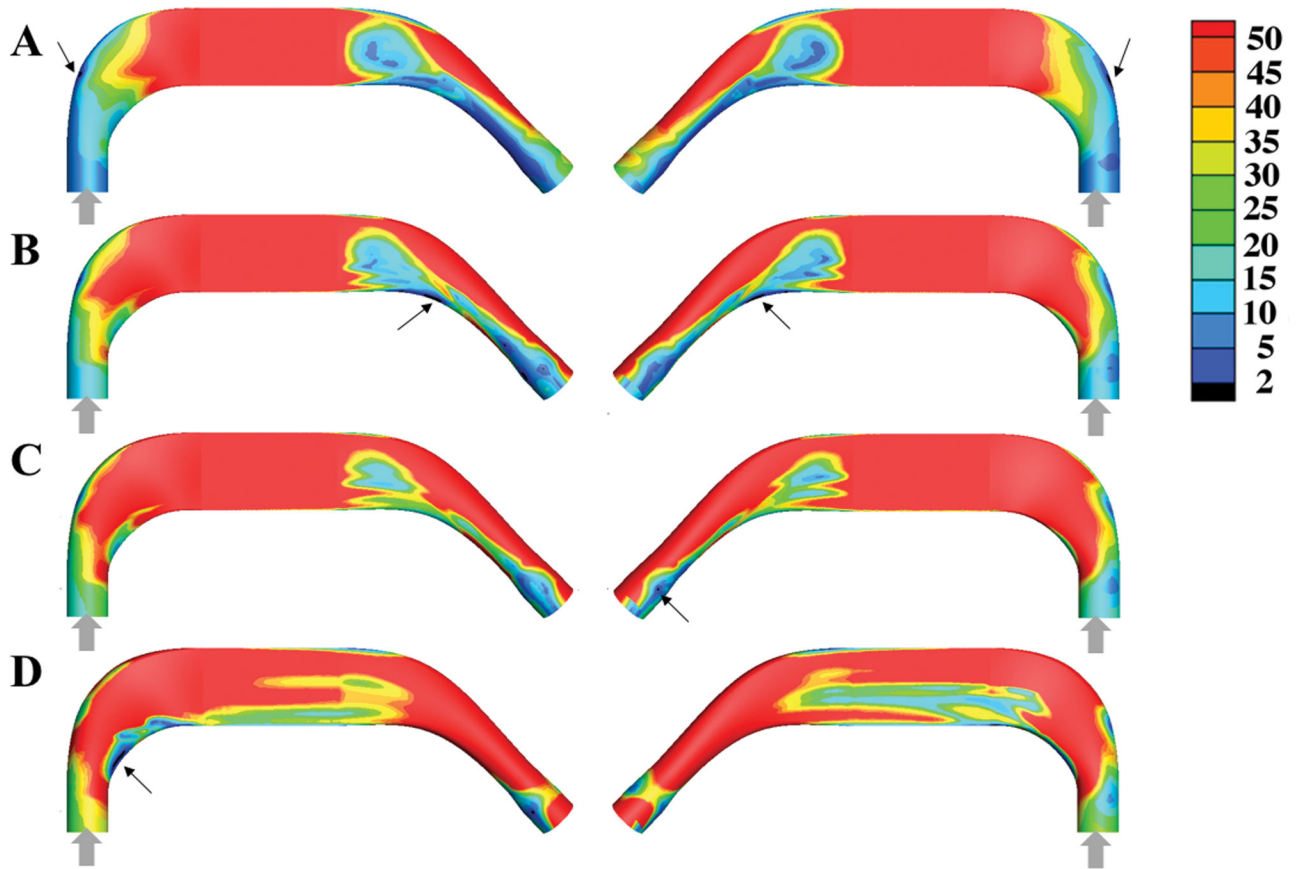
**Figure 7.**
For the simulation of *in vivo* conditions in Device B, two views are shown of the TAWSS map (Pa) for CFD simulations for flow through Device B with (A) 500 μm; (B) 750 μm; (C) 1000 μm; and (D) 2000 μm channel widths. Grey arrows indicate inflow region of the device, and black arrows indicate regions of locally low TAWSS.
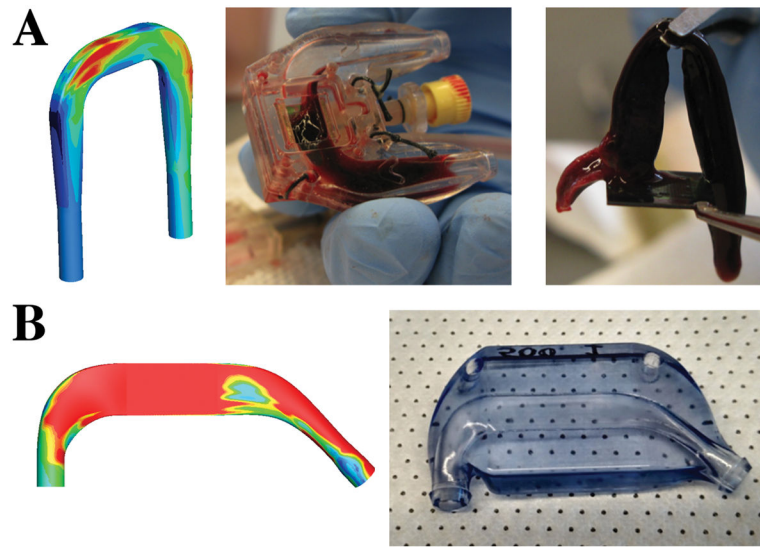
**Figure 8.**
A) Device A: TAWSS map (left); explanted (middle); extracted clot demonstrating a platelet-dominated portion (right). The location of the platelet-dominated portion of the clot was the inner wall of the distal curve, which corresponds with a simulated area of low mean WSS. B) Device B: TAWSS map (left); explanted Device B (right).

**TABLE 1**

Long-term anticoagulation strategies and outcomes for *in vivo* experiments.

| Implant | Long-term Anti-coagulation | Outcome |
|---|---|---|
| Device A | Heparin | Patent via US<br>No clot at explant Day 32 |
| Device A | Heparin | Patent via US<br>Clot at explant Day 24 |
| Device A | Heparin | Clot at Day 16 |
| Device A | Heparin | Clot at Day 11 |
| Device A | ASA | Patent via US<br>No clot at explant Day 30 |
| Device B_500 μm | ASA | Patent via US<br>No clot at explant Day 27 |
| Device B_500 μm | ASA | Patent via US<br>No clot at explant Day 28 |
| Device B_750 μm | ASA | Patent via US<br>No clot at explant Day 28 |
| Device B_750 μm | ASA | Patent via US<br>No clot at explant Day 30 |
| Device B_1000 μm | ASA | Patent via US<br>No clot at explant Day 28 |
| Device B_1000 μm | ASA | Patent via US<br>No clot at explant Day 30 |
| Device B_2000 μm | ASA | Patent via US<br>No clot at explant Day 31 |